UC San Diego

Title

Prolonged thermocline warming by near-inertial internal waves in the wakes of tropical cyclones.

Permalink

https://escholarship.org/uc/item/3q23k2s7

Journal

Proceedings of the National Academy of Sciences of USA, 120(26)

Authors

Gutiérrez Brizuela, Noel
Warner, Sally
Hughes, Kenneth
et al.

Publication Date

2023-06-27

DOI

10.1073/pnas.2301664120

Peer reviewed

Prolonged thermocline warming by near-inertial internal waves in the wakes of tropical cyclones

Noel Gutiérrez Brizuela[a,1] (ID), Matthew H. Alford[a] (ID), Shang-Ping Xie[a] (ID), Janet Sprintall[a] (ID), Gunnar Voet[a] (ID), Sally J. Warner[b] (ID), Kenneth Hughes[c] (ID), and James N. Moum[c] (ID)

Turbulence-enhanced mixing of upper ocean heat allows interaction between the tropical atmosphere and cold water masses that impact climate at higher latitudes thereby regulating air–sea coupling and poleward heat transport. Tropical cyclones (TCs) can drastically enhance upper ocean mixing and generate powerful near-inertial internal waves (NIWs) that propagate down into the deep ocean. Globally, downward mixing of heat during TC passage causes warming in the seasonal thermocline and pumps 0.15 to 0.6 PW of heat into the unventilated ocean. The final distribution of excess heat contributed by TCs is needed to understand subsequent consequences for climate; however, it is not well constrained by current observations. Notably, whether or not excess heat supplied by TCs penetrates deep enough to be kept in the ocean beyond the winter season is a matter of debate. Here, we show that NIWs generated by TCs drive thermocline mixing weeks after TC passage and thus greatly deepen the extent of downward heat transfer induced by TCs. Microstructure measurements of the turbulent diffusivity (κ) and turbulent heat flux (J_q) in the Western Pacific before and after the passage of three TCs indicate that mean thermocline values of κ and J_q increased by factors of 2 to 7 and 2 to 4 (95% confidence level), respectively, after TC passage. Excess mixing is shown to be associated with the vertical shear of NIWs, demonstrating that studies of TC–climate interactions ought to represent NIWs and their mixing to accurately capture TC effects on background ocean stratification and climate.

tropical cyclones | air–sea interactions | ocean heat content | ocean mixing | internal waves

Ocean turbulence regulates the ocean's internal stratification, circulation patterns, and poleward heat transport (1–3). Furthermore, modeling studies increasingly connect high-frequency weather disturbances to enhanced turbulent mixing that sustains the background air–sea thermal balance (4–7). Directly beneath the powerful winds of tropical cyclones (TCs), shear-driven turbulence entrains cold thermocline waters into the near-surface mixed layer (ML), thereby leaving cold ML wakes atop anomalously warm thermoclines (8–11). In the weeks following TC passage, cold sea surface temperatures (SSTs) help enhance local ocean heat uptake (OHU), causing the upper ocean to warm up and restratify back toward its climatological state (12–14). At the end of this process, subsurface warm anomalies that were mixed down during TC passage are effectively insulated from atmospheric influence and thus amount to a net increase in ocean heat content (OHC) (15–18). After being advected along isopycnals by large-scale currents, anomalies in OHC induced by TCs can reach the surface, release their heat into the atmosphere, and influence climate at remote locations (19–22).

Remote sensing estimates of the TC contribution to global OHU (total time rate of change in OHC) range roughly between 0.15 and 0.60 PW (see Bueti et al. (23) for an overview of major studies and methods). Whether that heat stays in the ocean for months or years, however, is a matter of debate. Assuming that warm anomalies induced by TCs stay fixed where they first appeared, Jansen et al. (24) estimated that as much as ∼70% of heat mixed down by TCs would be released locally to the atmosphere when the ML deepens during winter. However, rates of steric expansion inferred from sea surface height data in TC wakes suggest that anomalies in OHC induced by TCs mostly persist through the winter (15). Up to this point, it remains unclear which mechanisms are helping transfer warm anomalies below the winter ML and thus preserving TC-induced contributions to OHC.

Prolonged influence of TCs on values of thermocline turbulent diffusivity (κ) and resulting downward heat fluxes (J_q) would allow subsurface warm anomalies to deepen weeks after TC passage and thus keep them away from the winter ML. Near-inertial internal waves (NIWs), which are generated by fast-moving TCs (25, 26) and enhance

Significance

Powerful winds under tropical cyclones (TCs) mix thermal gradients in the upper ocean and thereby transfer heat down into the thermocline. Anomalous thermocline heat supplied by TC-driven mixing is eventually released back into the atmosphere, but whether subsequent impacts to climate are local or remote depends on the depth at which TCs deposit these warm anomalies. We use shipboard observations to demonstrate how near-inertial internal waves (NIWs) generated by TCs drive mixing that transfers ocean heat down across the thermocline weeks after TC passage. The magnitude of heat fluxes associated with NIWs suggests that this mechanism must be accounted for when assessing the impacts of TCs on ocean heat storage and climate.

[1]To whom correspondence may be addressed. Email: nogutier@ucsd.edu.

thermocline mixing (27–30), may well have such an effect. Cuypers et al. (31) used moored data of velocity and stratification after the passage of a tropical storm in the Indian Ocean to infer J_q and associated warming rates (T_t^{turb}, where the subscript t indicates a time rate of change) that result from vertical gradients in J_q (Eq. 4). Their analyses, which only cover the upper 100 m, rely on a fine-scale mixing parameterization (32, 33) that yields peaks in J_q along NIW shear layers and implies $T_t^{turb} \approx 0.015\,°C\ d^{-1}$ directly below NIW envelopes (31). Similarly, other studies have indirectly inferred the presence and effects of thermocline mixing by TC-generated NIWs (34, 35). However, sustained microstructure turbulence measurements are necessary to constrain the spatial and temporal extent to which TCs enhance κ and J_q and thereby understand the mechanisms responsible for preserving excess heat below the winter ML.

Knowing how, when, and where TCs drive ocean mixing is necessary to fully understand the TC contribution to OHC and subsequent impacts on climate (19, 21, 36, 37). Here, we compare microstructure estimates of κ and J_q before and after the passage of three major TCs. Our analyses confirm that thermocline values of κ and J_q are enhanced by TC-generated NIWs down to at least 300-m depth and up to three weeks after TC passage (the entire vertical and temporal span of our observations). Such prolonged mixing transfers heat between the seasonal and permanent thermoclines, thus deepening the reach of TC-induced warm anomalies and presumably extending their residence time in the ocean. Near-surface data also include increased J_q after TC passage, implying greater rates of heat uptake at the ocean surface. Lastly, we derive an empirical linear relation between thermocline NIW activity and κ and use it to infer the regional significance of thermocline warming by NIW-driven mixing in TC wakes. Overall, our analyses show that thermocline mixing by TC-generated NIWs must be represented in models to accurately assess the effects of TCs on OHC, the upper ocean circulation, and remote impacts to climate.

Results and Discussion

Shipboard measurements of subsurface ocean conditions before and after TC forcing in the Western Pacific Warm Pool were made onboard R/V Thomas G. Thompson between 20 August and 11 October 2018. The first half of our experiment was characterized by suppressed atmospheric convection (38), but TCs Mangkhut, Trami, and Kong-Rey moved by our study region during the second half (Fig. 1 A and B, SI Appendix, S1). The cumulative transfer of kinetic energy from winds into the ocean (ΔKE, Materials and Methods) calculated for two 30-d periods (Fig. 1 A and B) is reflected by vertical profiles of observed kinetic energy ($KE = \rho_0/2\|\mathbf{u}\|^2$, Fig. 1C) before and after TC passage. Ocean areas sampled before TC passage saw no gain in kinetic energy from winds (areas where $\Delta KE < 0$ in Fig. 1A), but regions sampled after TC passage gained $\Delta KE > 2 \times 10^5\ J\ m^{-2}$ (Fig. 1B). Only a fraction of ΔKE contributes to NIW generation, but rather than resolve the complicated dynamics that determine this energy transfer (39, 40), we point out that the translation speed of the three TCs was greater than the baroclinic mode-1 gravity wave speed over our study region (SI Appendix, Fig. S1). This implies that ocean currents in their wakes were dominated by NIWs (26, 41) and thus make it easy to identify the TCs' influence on upper ocean dynamics.

By comparing measurements made before and after the passage of TCs, we assess the ocean effects of TC forcing on timescales of days to weeks. To sort out spatial and temporal differences in the ocean response to TCs, our observations were grouped into one period representing conditions before TC passage (cyan lines in Fig. 1) and three depicting post-TC dynamics. The first set of post-TC measurements was located 250 km to the left of Mangkhut's track (Left side, orange lines), implying that NIWs observed there had most likely propagated south from regions where ΔKE peaked (8, 42). In contrast, the two later periods of post-TC observations represent ocean conditions across tracks (purple lines) and on the Right side of TC tracks (pink lines), thus including areas of greater ΔKE, ML deepening, and local NIW generation (39, 40). Ship tracks for each period are color-coded in Fig. 1 A and B, while the corresponding temporal coverages are compared to the timing of TC forcing in SI Appendix, Fig. S1. Time-depth sections of measured horizontal velocities ($\mathbf{u} = (u, v)$), their near-inertial component ($\|\mathbf{u}_{NI}\|$), κ, and the resulting J_q (Fig. 2) for each period reveal a clear contrast in NIW activity and mixing before and after TC passage.

TCs Mangkhut, Trami, and Kong-Rey moved across 135 °E on 12 September, 23 September, and 1 October, respectively (SI Appendix, Fig. S1 and Fig. 3C). Post-TC observations span the period between 21 September and 12 October, meaning that NIWs in our observations had time to disperse from each other, propagate away from their generation sites, and undergo refraction (43–45). Because NIWs can persist at a given site for ~25 d (46), the effects of the three TCs are likely superimposed in parts of our record. Therefore, our measurements are representative of the Tropical Western Pacific at the height of the TC season rather than of the ocean's long-term response to a single TC.

Upper Ocean Conditions Before and After TC Forcing. Upper ocean conditions after the passage of TCs are characterized by elevated mean values of KE, κ, J_q, and shear variance (Fig. 1 C–F) compared to ocean conditions before TCs (cyan lines). Note that 95% confidence intervals for the time-depth means of κ and J_q in Table 1 are shown separately for the near-surface (0 to 50 m depth, white rows) and thermocline levels (50 to 250 m, turquoise rows), revealing that J_q increased after TC passage by factors in the ranges [1.8, 21.4] and [1.7, 4.8] at the near-surface and thermocline levels. Low values of J_q between 50 and 70 m for all periods in Fig. 1E indicate that turbulent heat transfer in the near-surface was relatively independent of transfer within the thermocline. In other words, there are two separate mixing processes happening above and below the ML base days to weeks after TC passage, and near-surface restratification is helping insulate thermocline heat, a necessary condition for net OHC to increase after TC passage (17).

Vertical profiles of J_q in Fig. 1E are consistent with increased OHU in the TC wake, while thermocline data further point to enhanced heat transfer across 150-m depth or between the seasonal and permanent thermoclines. The mean heat flux convergence and resulting warming rates T_t^{turb} are ~0.03 °C d^{-1} in the upper 50 m, while thermocline measurements reveal contiguous layers with warming/cooling rates reaching ± 0.015°C d^{-1} (Fig. 1G, Materials and Methods). These values contrast with observations made before TC passage, when maximum values of T_t^{turb} were roughly 25% of those measured after TC forcing (Fig. 1G). Overall, this evidence points to increased local OHU after TC forcing and prolonged deepening of upper thermocline heat, which would presumably reduce the amount of heat that will be locally lost to the atmosphere during winter.
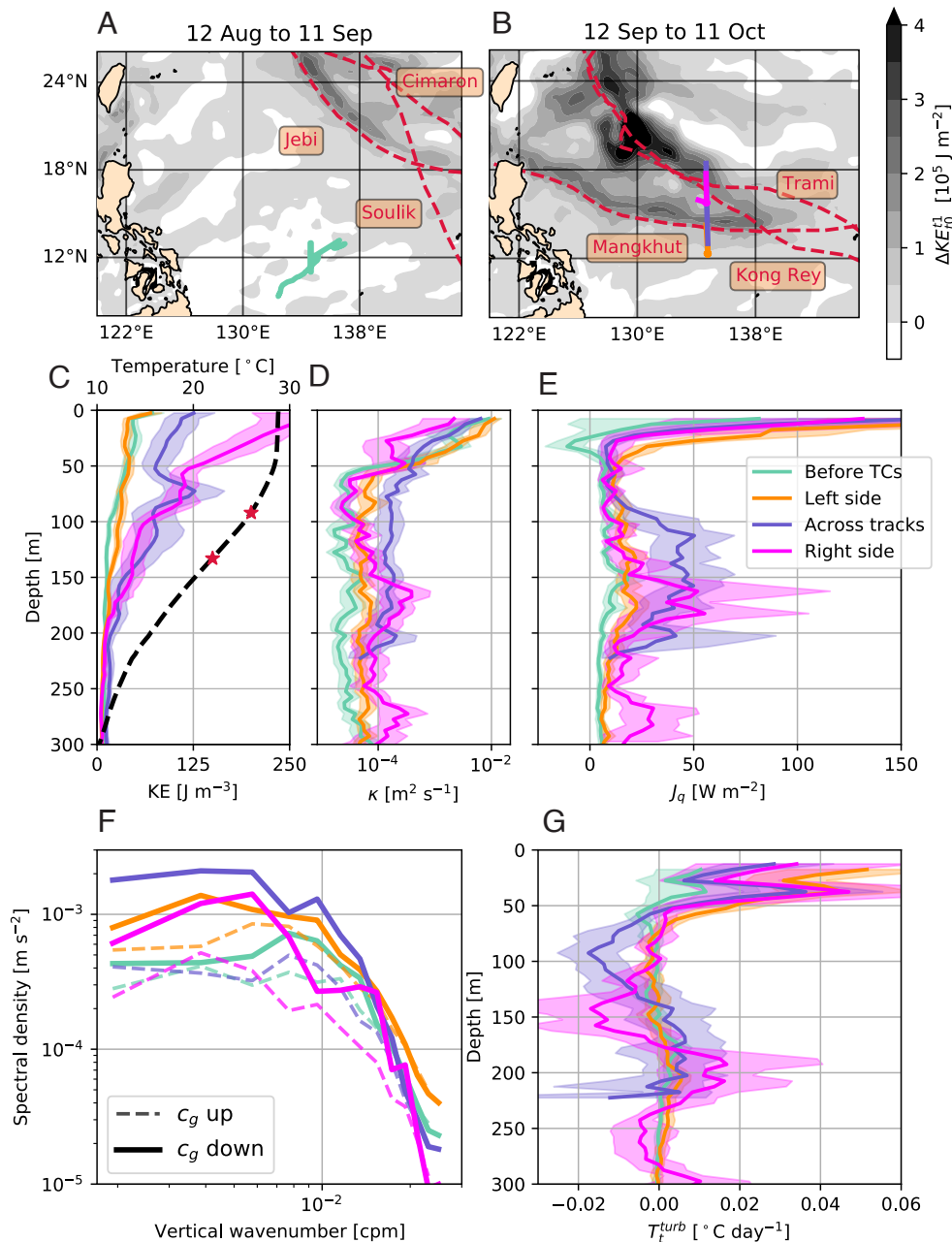
Fig. 1. Ocean effects of wind forcing by TCs. (*A* and *B*) ΔKE integrated over the periods noted in 2018. Mean vertical profiles and 95% confidence intervals of (*C*) KE, (*D*) κ, and (*E*) J_q for each of the four periods defined in Fig. 2. (*C*) shows the mean $T(z)$ across all periods (dashed black line, upper axis), while red stars mark the 22 and 26 °C isotherms. (*F*) vertical wavenumber spectra of shear are shown in dashed and solid lines for rotation associated with upward- and downward-propagating internal wave energy, respectively. (*G*) T_t^{turb} computed from the convergence of smoothed profiles of J_q in (*E*).

Observed Collocation of NIWs, κ, and J_q. Time-depth sections of $\mathbf{u}$, $\mathbf{u}_{\mathrm{NI}}$, κ, and J_q in Fig. 2 indicate that the observed increase in thermocline values of κ and J_q was associated with TC-generated NIWs. $\|\mathbf{u}_{\mathrm{NI}}\|$ rarely reached 0.15 m s^{-1} before TC passage (Fig. 2 *E* and *I*), but downward-propagating envelopes where $\|\mathbf{u}_{\mathrm{NI}}\| > 0.15$ m s^{-1} are evident in all post-TC measurements. More importantly, NIW envelopes are collocated with areas of enhanced κ and J_q (Fig. 2 *F–H* and *J–L*). This collocation continues down to 300 m, as deep as our microstructure measurements go, but is likely to continue at greater depths as NIWs propagate into the deep ocean.

Changes in rotary wavenumber spectra of shear (Fig. 1*F*, *Materials and Methods*) before and after TC passage show a significant increase in variance associated with TC-generated

internal waves. Shear associated with downward-propagating internal wave modes (c_g down, Fig. 1*F*) increased after TC passage and at virtually all scales, while upward-propagating internal wave modes (c_g up, Fig. 1*F*) did not consistently increase their shear variance. Evidence of increased shear due to downward-propagating NIWs may explain the collocation between mixing and NIWs in Fig. 2 *F–H* and *J–L*, as shear instability is known to be the leading driver of mixing within NIW envelopes (27–29).

A meridional transect across the wakes of TCs Mangkhut, Trami, and Kong-Rey (Fig. 3 spans the across-TC-tracks period) reveals complex variations in NIW properties and mixing that result from patterns in NIW generation and propagation since TC passage. Tilted bands of alternating signs in v and v_{NI}
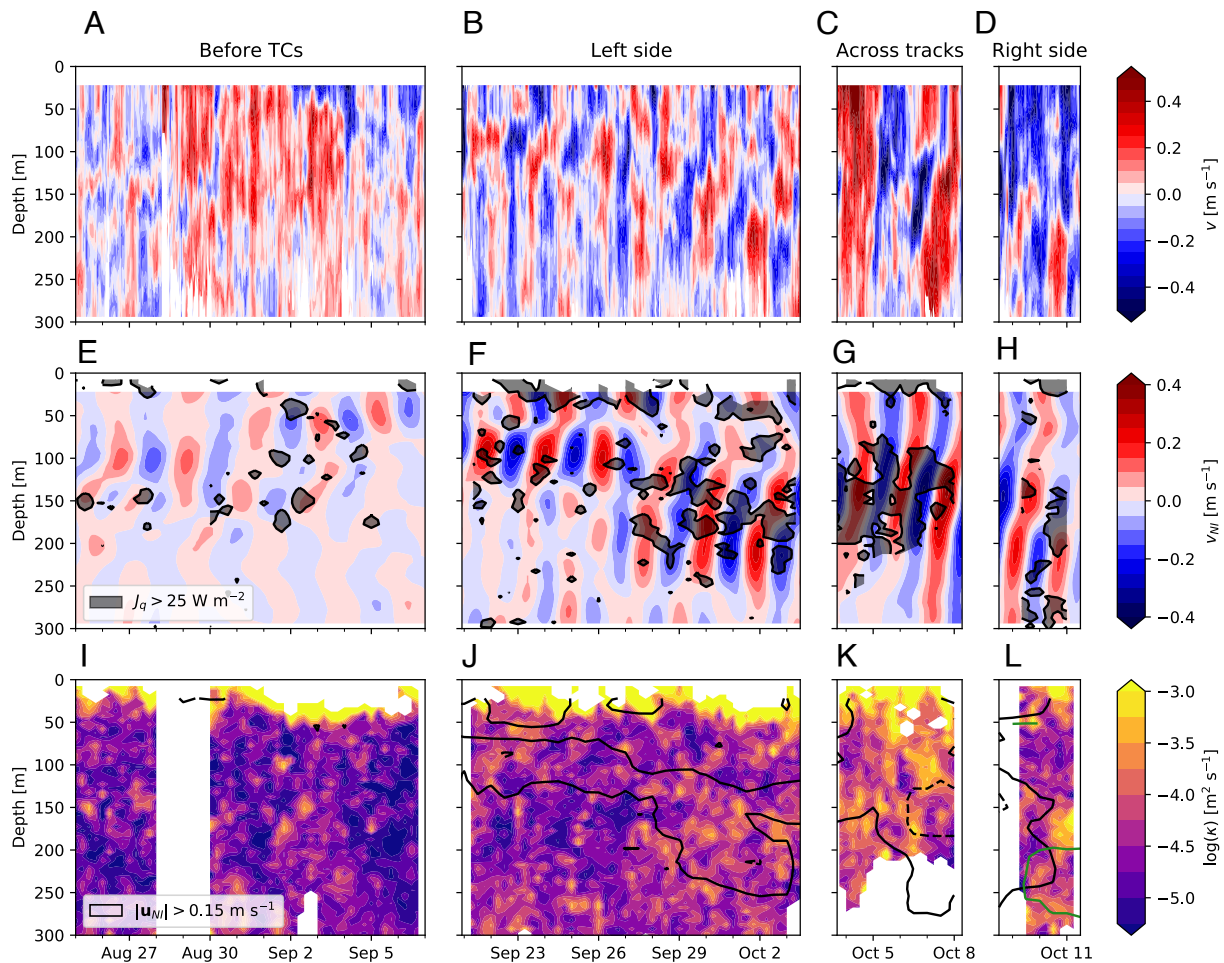
Fig. 2. Upper ocean conditions before and after the passage of three major TCs. Color shading shows (*A–D*) observed velocities *v*, their (*E–H*) bandpass-filtered component v_{NI}, and associated (*I–L*) 12-h averages of κ. Gray hatching in (*E–H*) outlines areas where 8-h averages of J_q are greater than 25 W m^{-2}. Black contours in (*I–L*) outline areas where $\|\mathbf{u}_{\mathrm{NI}}\|$ is greater than (solid) 0.15 and (dashed) 0.3 m s^{-1}. Each column represents one of the periods whose temporal averages are shown in Fig. 1.

(Figs. 3*A* and 2*G*) are more intense and dominated by greater vertical scales at the northern end of the transect, which features more recent TC forcing than the southern end. Three distinct maxima in near-surface $\|\mathbf{u}\|$ are located near 13.8, 15.8, and 17.8°N (Fig. 3*B*) and likely associated with the passage of TCs Mangkhut, Kong-Rey, and Trami, which crossed 134.7°E near 14.1, 16.5, and 17.1°N roughly 23, 5, and 14 d before we sampled their respective latitudes (Fig. 3*C*). Thermocline $\|\mathbf{u}\|$ was as high as 1.1 m s^{-1} directly below mesoscale layers where shear squared ($S^2 = \|\frac{\partial \mathbf{u}}{\partial z}\|^2$) peaks and thus creates a favorable environment for enhanced turbulence (Fig. 3 *C* and *D*).

Elevated mean values of thermocline J_q after TC passage (Fig. 1*E* and Table 1) were largely set by relatively few intermittent events with $J_q > 100$ W m^{-2} that happened near local peaks in S^2 (Fig. 3*C*). We assess the impact of S^2 on J_q by calculating the Richardson number $Ri = N^2/S^2$ and outlining areas where $Ri < 0.5$ (gray contours in Fig. 3*D*). Here, N is the buoyancy frequency, and while the canonical threshold for shear instability is $Ri < 0.25$, we use a higher value to compensate for the vertical resolution of $\mathbf{u}$. Notice that the background value of J_q is negligibly small, but sporadic patches of increased J_q are collocated with gray contours in Fig. 3*D*. This collocation is evidence that enhanced mixing resulted from shear instability in NIWs.

Regional Variations in NIW Activity and Mixing. To generalize our time- and location-specific measurements, we assume that empirical relations between observed $\|\mathbf{u}_{\mathrm{NI}}\|$ and κ (Fig. 4 *A* and *B*) are representative of those in other areas impacted by the same TCs. This way, we use HYCOM's representation of thermocline $\|\mathbf{u}_{\mathrm{NI}}\|$ (*SI Appendix*) to inform the distribution of NIW activity throughout the Western Pacific and infer associated patterns in κ and thermocline mixing (Fig. 4 *C* and *D*). Even though $\|\mathbf{u}_{\mathrm{NI}}\|$ is only an indirect proxy for turbulence and NIWs drive enhanced mixing through their effect on S^2 and Ri (Fig. 3 *C* and *D*), extending the observed relation between $\|\mathbf{u}_{\mathrm{NI}}\|$ and κ helps us to broadly assess the impacts of TC-generated NIWs on the regional ocean heat budget.

Observed 4-d averages of thermocline κ and $\|\mathbf{u}_{\mathrm{NI}}\|$ covaried during our experiment (Fig. 4*A*). In fact, the linear relation

$$\kappa = a\|\mathbf{u}_{\mathrm{NI}}\| + b, \qquad [1]$$

yields a correlation coefficient $r = 0.64$ when $a = 33 \pm 5 \times 10^{-5}$ and $b = 0.9 \pm 0.9 \times 10^{-5}$ (Fig. 4*B*, 95% CI). A comparison between HYCOM's representation of NIW activity ($\|\mathbf{u}_{\mathrm{NI}}^{\mathrm{HYCOM}}\|$) and 2 y-long moored records from our study region shows that HYCOM can roughly reproduce temporal patterns in $\|\mathbf{u}_{\mathrm{NI}}\|$ but can underestimate its value below 100 m (*SI Appendix*, Figs. S2 and S3). After noting this, we used $\|\mathbf{u}_{\mathrm{NI}}^{\mathrm{HYCOM}}\|$ and the linear
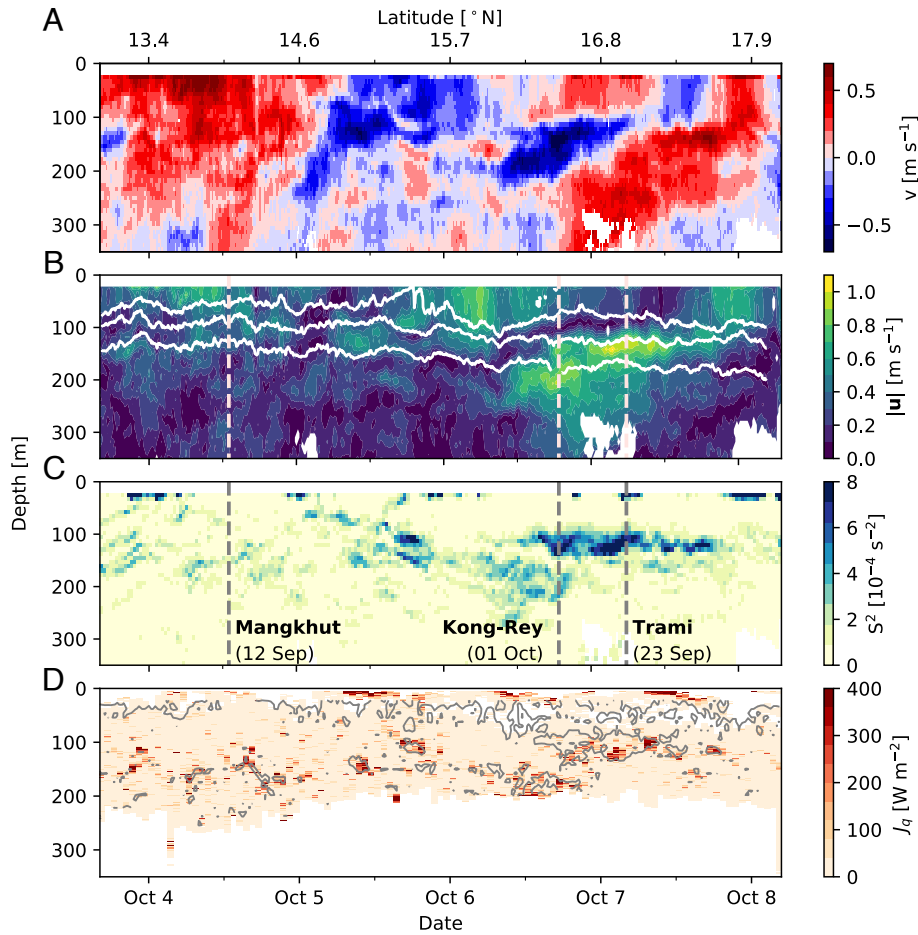
A

Fig. 3. NIW activity, shear, and turbulence across TC tracks. Shipboard data show (*A*) *v*, (*B*) ‖**u**‖, (*C*) S^2, and (*D*) J_q in color. White contours in (*B*) track the 22, 26, and 28 °C isotherms, while gray contours in (*D*) show areas where $Ri = N^2/S^2 < 0.5$. Vertical dashed lines Fig. 3 *B* and *C* indicate the approximate latitudes and dates (text in parentheses) at which TC tracks crossed 134.7°E.

relation in Fig. 4*A* to estimate κ and J_q during our experiment in the Western Pacific (Fig. 4 *C* and *D*).

To emphasize the long timescales of NIW-driven mixing, HYCOM-based estimates of κ and J_q are shown in Fig. 4 *C* and *D* as 30-d averages between 12 September and 11 October (the same period used for ΔKE in Fig. 1*B*). To facilitate interpretation of their climate significance, κ and J_q were interpolated onto the 22 and 26 °C isotherms. Results for the 22 °C isotherm are shown in Fig. 4 *C* and *D*, while results at the 26 °C level are shown in

Table 1. Statistical summary of four periods of observation

	N	$\langle \kappa \rangle$ [10^{-5} m^2 s^{-1}]	J_q
Before TCs	1,273	[125 - 241]	[3 - 13]
		[3 - 3]	[7 - 8]
Left side	1,635	[243 - 337]	[40 - 56]
		[6 - 7]	[14 - 15]
Across tracks	841	[133 - 201]	[26 - 44]
		[16 - 20]	[30 - 35]
Right side	306	[45 - 94]	[25 - 56]
		[9 - 12]	[18 - 23]

Based on a total of *N* individual casts, 95% confidence intervals for the average κ and J_q were computed for the near-surface (depth < 50 m, white rows) and thermocline (50 to 250 m depth, green rows) layers during each of the periods defined in Fig. 2. Vertical variations in κ and J_q are plotted with confidence intervals in Fig. 1 *D* and *E*.

SI Appendix, Fig. S4 *a* and *b*, and a time series of the T_t^{turb} that results from differences between the two levels is shown in *SI Appendix*, Fig. S4*C*. The 22 °C isotherm was chosen because it roughly separates between hotter water masses that take up heat from the atmosphere and colder ones that release their heat into the atmosphere (1). Similarly, the 26 °C isotherm was chosen because it approximately marks an SST threshold at which air–sea fluxes can power TC intensification (47, 48).

Regional estimates of thermocline κ have local peaks along the right sides of TC tracks (dashed lines in Fig. 4*D*), consistent with the asymmetry of NIW generation by TCs (42). While the influence of TCs Mangkhut, Trami, and Kong-Rey is most prominent, κ is also 2 to 3 times greater than the background along the track of TC Jebi (blue dashed line), which passed by this area near 1 September. Similar patterns are observed in J_q, which is as high as 35 W m^{-2}. These values are roughly consistent with observations, where mean values of J_q at the 22 °C isotherm are approximately 20, 40, and 20 W m^{-2} for the *Left-side*, across-TC-tracks, and *Right-side* periods, respectively (Fig. 1*E*).

To assess the climatic relevance of our results, we focus on values of J_q inside the $10^\circ \times 6^\circ$ dashed box in Fig. 4*D*. There, the area-averaged NIW-driven J_q across the 22 °C isotherm was 20.5 ± 3.0 W m^{-2}, which is roughly 5% greater than across the 26 °C isotherm (*SI Appendix*, Fig. S4 *A* and *B*) and ~80% of the climatological surface heat flux for September ($\approx$25 W m^{-2}). The difference between J_q at 22 and 26 °C, which is small
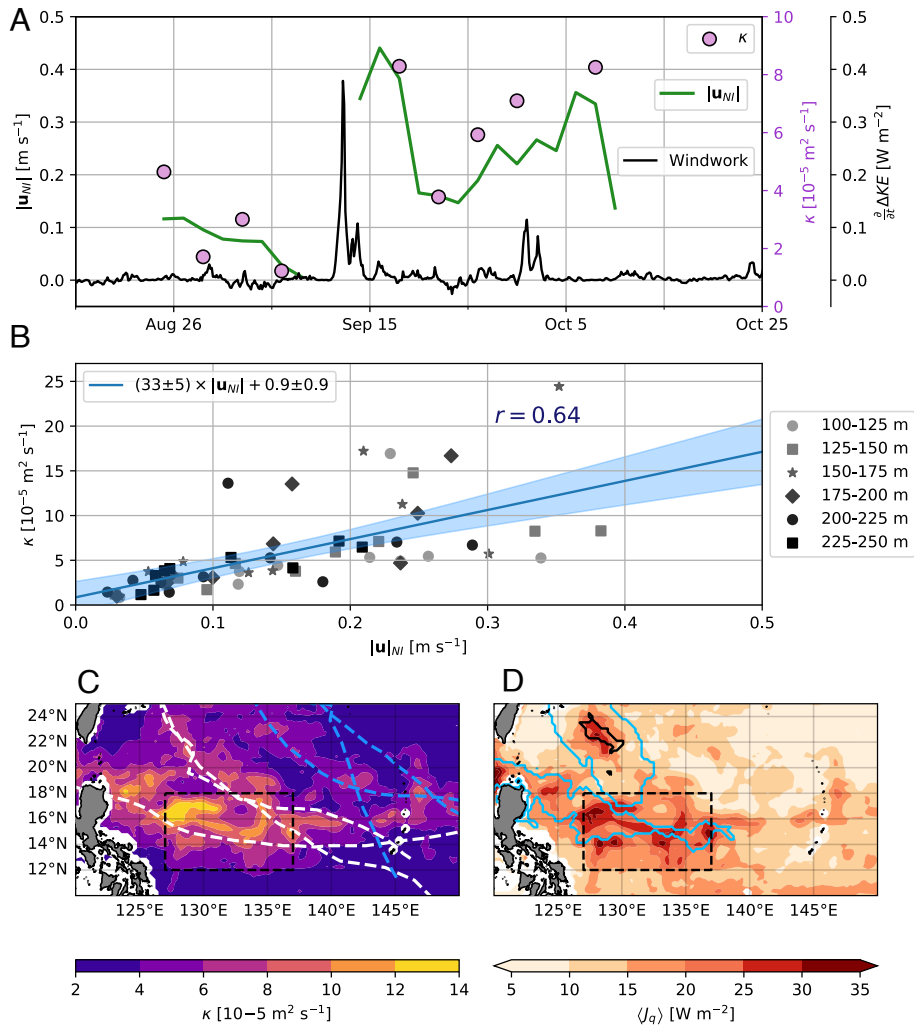
Fig. 4. NIW activity, its relation to κ, and regional effects. (*A*) 4-d averages of $\|\mathbf{u}_{NI}\|$ (green line) and κ (pink circles) observed between 125 and 150 m. Windwork $\frac{\partial}{\partial t}\Delta KE$ at the mooring site is shown in black. (*B*) Linear fit on 4-d averages of observed $\|\mathbf{u}_{NI}\|$ and κ at different depths ($r = 0.64$). Mean values of (*C*) κ and (*D*) J_q at the 22 °C isotherm between September 12 and October 11 inferred from $\|\mathbf{u}_{NI}^{HYCOM}\|$. Dashed lines in blue and white show TC tracks as in Fig. 1 *A* and *B*. The blue contour in (*D*) shows areas of SST cooling >1 °C induced by TCs, while the black contour denotes an area where z_L was deeper than the 22 °C isotherm. The dashed box is the area whose averages are described in the main text.

compared to the magnitude of J_q, would presumably cool the water between these isotherms at a rate ≈ 0.01°C month^{-1} (*SI Appendix*, Fig. S4*C*, Eq. **4**), while the remaining J_q remains available to warm the ocean below 22 °C.

Integrated within the dashed box in Fig. 4*D*, NIW-driven J_q transfers $\sim$0.015 PW across the 22 °C isotherm, which is between 2.5 and 10% of the global TC contribution to OHU (15, 16, 18). Furthermore, this downward heat flux is $\sim$2% of the northward Pacific heat transport out of the tropics (49, 50) and $\sim$16% of the contribution by eddies (51). Considering that these estimates account for only a small fraction of the area impacted by the three TCs in this study, our analyses highlight the importance of NIWs in shaping the TC contribution to OHC and climate.

SST Cooling and TC-Driven Mixing. Previous estimates of the TC contribution to OHC have used satellite measurements of SST cooling behind TCs to infer the TC-induced κ via a characteristic mixing depth z_L. This method, exemplified in Fig. 5*A*, often defines z_L as the depth above which the average pre-TC temperature is equal to the SST after TC passage (T_{TC}). Assuming a mixing timescale $t_{mix} \sim 24$ h to represent the

duration of the forced stage, turbulence is then roughly quantified as $\kappa \approx z_L^2/t_{mix}$ (16, 20, 52). While this approach is physically sound and has proven useful to parameterize TC-driven mixing, it gives the impression that TC-driven mixing only acts to impact SST via ML deepening and that it only does it during the forced stage of TCs. However, observations in Figs. 1*E* and 2 *E–H* show that turbulence in TC-generated NIWs drives a prolonged downward transfer of heat across the thermocline (Fig. 5*B*). If the contribution of TCs to ocean heat transport and remote climate is in fact determined by the amount of heat they transfer to water masses colder than the local wintertime SST (24), quantifying J_q in the thermocline weeks to months after TC passage is essential to assessing the net impact of TCs on OHC and climate (Fig. 5).

Spatial patterns in SST cooling and z_L are not indicative of the distribution of NIW activity and thermocline mixing. Blue contours in Fig. 4*D* outline areas where SST cooling in TC wakes exceeded 1 °C, while black contours indicate areas where z_L reached below the 22 °C isotherm (*Materials and Methods*). Differences between these contours and our estimates of J_q (Fig. 4*D*) show that SST-based techniques would indicate that no heat was transferred across the 22 °C along the track
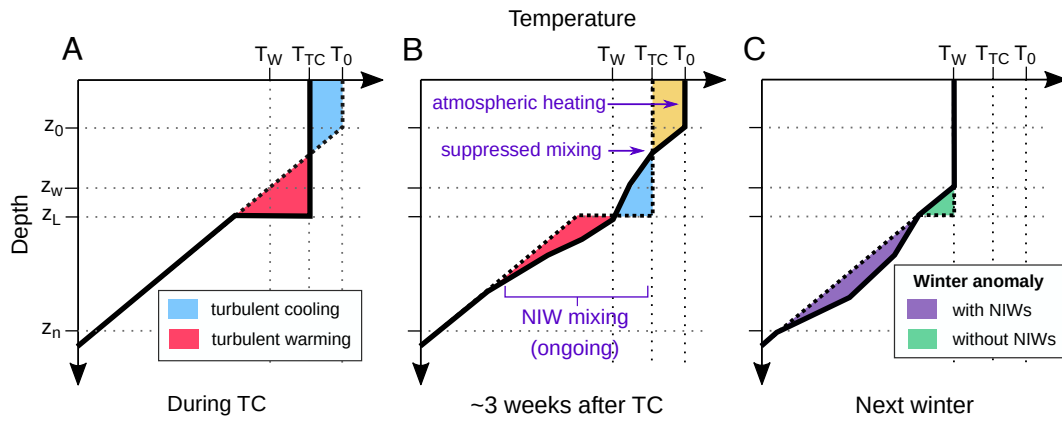
Temperature

Fig. 5. Schematic description of short-term and long-term changes in $T(z)$ induced by TC forcing. The solid lines in each panel show (A) ML deepening that happens under TC winds, (B) the partial effect of J_q enhanced by NIWs, and (C) the cumulative effect of NIWs at the end of the TC season. T_0, T_{TC}, and T_w are the pre-TC, post-TC, and wintertime values of SST. Likewise, z_0 is the pre-TC ML depth, z_W is the wintertime ML depth, z_L is the mixing depth inferred from SST, and z_n is the depth below which the NIW-induced J_q is negligible.

of TC Mangkhut. The comparison yields similar results at the 26 °C level (*SI Appendix*, Fig. S4*B*), highlighting how SST cooling and the prolonged NIW-driven mixing detailed by our observations are complementary but quite different facets of TC-driven mixing.

A schematic in Fig. 5 summarizes the different stages of mixing driven by TCs and their distinct impacts to upper ocean stratification. SST cooling results from mixing at the ML base during the forced stage of TCs (Fig. 5*A*) and tends to be collocated with ΔKE (8). In contrast, the 3D distribution of NIWs is impacted by TC forcing, background stratification, and ocean currents with horizontal scales ∼25 km and greater (44, 45). Without a proper representation of NIWs and their mixing, ocean models are likely to underestimate the depth of anomalous OHC induced by TCs (Fig. 5*B*) and thereby misallocate anomalous air–sea fluxes in subsequent seasons and years (Fig. 5*C*). Two year-long comparisons between modeled and observed $\|\mathbf{u}_{NI}\|$ in *SI Appendix*, Figs. S2 and S3 show that HYCOM (horizontal resolution $1/12 \times 1/12°$) underestimates $\|\mathbf{u}_{NI}\|$ with increasing depth, yielding annually averaged values >30% lower than observations below 150 m. This is likely due to the low vertical resolution (50 to 100 m) of HYCOM's permanent thermocline, suggesting that high-resolution model configurations and NIW-specific parameterizations alike (5, 53) are needed to accurately reproduce the TC contribution to OHC and meridional heat transport.

Conclusion

Much like the phenomenon in which mixing at the ML base cools the surface and heats up the seasonal thermocline during the forced stage of TCs (Fig. 5*A*), NIW-driven mixing in the thermocline cools waters directly beneath the ML base and warms the permanent thermocline for weeks after (Figs. 1*G* and 5*B*). Microstructure estimates of J_q demonstrate that NIW-driven mixing can help transfer > 20 W m^{-2} across the 22 °C isotherm for weeks after TC passage (Fig. 1*E* and 4*D*). This prolonged thermocline mixing does not directly impact SST or air–sea fluxes because a minimum in J_q at the base of the post-TC ML insulates the thermocline from near-surface processes (Fig. 1*E*). Instead, NIW-driven mixing is important to understand the TC impact on ocean stratification because it helps cool the seasonal thermocline and warm the deep ocean (Fig. 5*B*) during fall, when

the tropical OHC peaks. Heat transfer across the 22 °C isotherm by TC-generated NIWs (Fig. 4*D*) ensures that heat anomalies will be advected toward the midlatitudes or the Equatorial Cold Tongues (1), as opposed to being ventilated locally when the ML deepens during winter (Fig. 5*C*).

Enhanced thermocline κ and J_q weeks after TC passage result from vertical shear in TC-generated NIWs that propagate into the deep ocean (Figs. 2 *E–L* and 3*D*). This mechanism is likely to unfold throughout the TC season and over vast regions of the Western Pacific Warm Pool (Fig. 4*D*). Given these scales, mixing by TC-generated NIWs may help explain TC–climate interactions noted in models and observations (21, 22, 54). Inclusion of this previously unrecognized mechanism in climate models constitutes a great technical challenge, as full representation of TC-generated NIWs and their mixing requires high spatial resolution (55, 56), fast air–sea coupling, and specialized parameterizations (5, 53). Likewise, further microstructure measurements of κ and J_q will be necessary to constrain the fate of warm anomalies deepened by NIW-driven mixing, as this cannot be retrieved from SST, sea surface height, or even in situ temperature measurements that fail to distinguish turbulent warming from downwelling or horizontal advection.

Materials and Methods

Shipboard Data. Horizontal velocities **u** (Figs. 2 *A–D* and 3*B*) were measured using a hull-mounted, 75-kHz acoustic Doppler current profiler (ADCP) and were processed using a third-order Butterworth filter within the frequency range [*0.7f, 1.3f*] to extract their near-inertial component $\mathbf{u}_{NI}$ (Fig. 2 *E-H*), where f is the mean inertial frequency for locations sampled. The same filter was used to compute $\mathbf{u}_{NI}$ from moored records (*SI Appendix*, Fig. S2) and HYCOM output. Vertical wavenumber spectra of shear (Fig. 1*F*) were computed after applying WKB-stretching and scaling procedures in ref. 57, for which monthly stratification data from ARGO (58) were used.

Because the ship was only static from 21 September to October 3 and from October 9 to October 12, bandpass filters used to calculate $\|\mathbf{u}_{NI}\|$ when the ship moved across TC wakes are likely to underestimate $\|\mathbf{u}_{NI}\|$. While ship motion induces a bias in the perceived phase propagation of NIWs (28, 59), small-scale spatial variations in $\|\mathbf{u}_{NI}\|$ can further bias the results of bandpass filtering. Cross-track variations in $\|\mathbf{u}_{NI}\|$ follow the length scale ∼100 km or twice the maximum wind radius of TCs (25, 26), but our ship moved at a cross-track velocity of up to 250 km for every inertial period (Fig. 3). Sampling at that speed, a 100 km-long peak in $\|\mathbf{u}_{NI}\|$ would appear in measurements as an oscillation with frequency >2f. This may be the case for some of the local peaks near 150 m in

Fig. 3*B*, where $\|\mathbf{u}\|$ goes from 0.4 to 0.9 m s^{-1} and back to 0.4 m s^{-1} in ~150 km, or little more than half an inertial period.

More than 4,000 individual vertical profiles of temperature (T), stratification (N^2), and the turbulent dissipation rate (ε) were obtained using the Chameleon microstructure profiler (60), which was deployed from the stern of R/V Thomas G. Thompson. Following (61), we used 3-h averages of ε and N^2, and set $\Gamma = 0.2$ (62, 63) to compute κ as

$$\kappa = \Gamma \frac{\varepsilon}{N^2}. \qquad [2]$$

Likewise, turbulent heat fluxes J_q were computed as

$$J_q = \rho_0 c_p \kappa \frac{\partial T}{\partial z}, \qquad [3]$$

while estimates of the turbulent warming rate T_t^{turb} are given by

$$T_t^{\text{turb}} = \frac{\partial}{\partial z}\left(\kappa \frac{\partial T}{\partial z}\right) = \frac{-1}{\rho_0 c_p} \frac{\partial J_q}{\partial z}. \qquad [4]$$

Here, $\rho_0 = 1024$ kg m^{-3} is the reference density of seawater and $c_p = 4.1 \times 10^3$ J K^{-1} kg^{-1} is the heat capacity. J_q and T'_{turb} were computed using hourly averages of the vertical temperature gradient $\frac{\partial T}{\partial z}$ and κ as shown in Fig. 3*D*, and later averaged to the temporal periods specified in Figs. 1, 2, 4, and Table 1. Confidence intervals in Fig. 1 and Table 1 were computed via bootstrapping.

Reanalysis Data. Data from the atmospheric ERA5 (64) and oceanic HYCOM (65) reanalyses provide context for shipboard observations and help inform their large-scale implications. We computed the cumulative transfer of kinetic energy into the ocean $\Delta KE = \int \tau \cdot \mathbf{u}_{surf} \, dt$ as a proxy for net forcing, assuming that a fraction of ΔKE becomes available for NIW generation (Fig. 1 *A* and *B*). Here, τ and $\mathbf{u}_{surf}$ are given 3-h data of wind stress and surface velocities from ERA5 and HYCOM respectively, while the dates t_0 and t_1 used are indicated as titles on top of Fig. 1 *A* and *B*.

$\mathbf{u}_{\text{NI}}^{\text{HYCOM}}$ was obtained by applying a third-order Butterworth bandpass filter to the model's velocity output using the local frequency range [*0.7f, 1.3f*]. Values of $\|\mathbf{u}_{\text{NI}}^{\text{HYCOM}}\|$ were computed for multiple vertical levels and later validated by comparing them against corresponding measurements from two year-long moored records within our area of observations (*SI Appendix*, Figs. S2 and S3).

Thirty-day averages of κ in Fig. 4*C*, *SI Appendix*, Fig. S4A were calculated by interpolating 4-d averages of $\|\mathbf{u}_{\text{NI}}\|$ on to the depth of the 22 °C isotherm, applying the linear fit described in Fig. 4*B* to obtain κ, and averaging the results between 12 September and 11 October. Corresponding values of J_q (Fig. 4*D*) were calculated as $c_p \rho_0 \kappa \frac{\partial T}{\partial z}$ and averaged within the same period, where $\frac{\partial T}{\partial z}$ is the local vertical temperature gradient in HYCOM.

TC Tracks and Induced SST Cooling. TC track and intensity data are from the US Navy's Joint Typhoon Warning Center (JTWC) and summarized in *SI Appendix*, Fig. S1. TCs' potential for NIW generation was assessed using the ratio U_{storm}/c_g, where U_{storm} is the TC translation speed and c_g is the local baroclinic mode-1 gravity wave speed roughly 3.2 m s^{-1}, (66), which was computed using ARGO climatology data (58) and assuming constant stratification beneath 2,000 m.

SST cooling induced by TCs was computed as the difference between SST averages 3 to 10 d before and 1 to 4 d after TC passage (56) with daily SST data from ERA5. SST cooling was computed for every location within 200 km of TC tracks and corresponding dates of TC passage were defined as the dates of closest proximity to the TC eye. Results were used to plot the blue contours in Fig. 4*D*), which highlight areas where SST cooling from TCs Mangkhut, Trami, or Kong-Rey was greater than 1 °C. Moreover, the characteristic mixing depth z_L was computed using HYCOM temperature stratification data, and areas where z_L went deeper than the pre-TC 22 °C isotherm are shown as black contours in Fig. 4*D*, *SI Appendix*, Fig. S4C.

Data, Materials, and Software Availability. Shipboard data have been deposited in Zenodo (https://zenodo.org/record/7601193) (67).

Author affiliations: aScripps Institution of Oceanography, University of California, San Diego, La Jolla, CA 92093; bEnvironmental Studies Program and Physics Department, Brandeis University, Waltham, MA 02453; and cCollege of Earth, Ocean, and Atmospheric Sciences, Oregon State University, Corvallis, OR 97331

1. R. M. Holmes, J. D. Zika, M. H. England, Diathermal heat transport in a global ocean model. *J. Phys. Oceanogr.* **49**, 141–161 (2019).
2. A. Ganachaud, C. Wunsch, Improved estimates of global ocean circulation, heat transport and mixing from hydrographic data. *Nature* **408**, 453–457 (2000).
3. J. A. MacKinnon *et al.*, Climate process team on internal wave-driven ocean mixing. *Bull. Am. Meteorol. Soc.* **98**, 2429–2454 (2017).
4. B. Qiu, S. Chen, P. Hacker, Synoptic-scale air-sea flux forcing in the western North Pacific: Observations and their impact on SST and the mixed layer. *J. Phys. Oceanogr.* **34**, 2148–2159 (2004).
5. M. Jochum *et al.*, The impact of oceanic near-inertial waves on climate. *J. Clim.* **26**, 2833–2844 (2013).
6. S. Zhang *et al.*, Impact of having realistic tropical cyclone frequency on ocean heat content and transport forecasts in a high-resolution coupled model. *Geophys. Res. Lett.* **42**, 5966–5973 (2015).
7. M. T Luongo, N. Brizuela, I. Eisenman, S.-P. Xie, Retaining short-term variability reduces biases in wind stress overriding simulations. Authorea Preprints (2023).
8. J. F. Price, Upper ocean response to a hurricane. *J. Phys. Oceanogr.* **11**, 153–175 (1981).
9. R. K. Mrvaljevic *et al.*, Observations of the cold wake of Typhoon Fanapi (2010). *Geophys. Res. Lett.* **40**, 316–321 (2013).
10. H. Zhang *et al.*, Net modulation of upper ocean thermal structure by Typhoon Kalmaegi (2014). *J. Geophys. Res. Oceans* **123**, 7154–7171 (2018).
11. T. M. S. Johnston, D. L. Rudnick, N. Brizuela, J. N. Moum, Advection by the north equatorial current of a cold wake due to multiple typhoons in the western pacific: Measurements from a profiling float array. *J. Geophys. Res. Oceans* **125**, e2019JC015534 (2020).
12. J. F. Price, J. Morzel, P. P. Niiler, Warming of SST in the cool wake of a moving hurricane. *J. Geophys. Res. Oceans* **113**, e2007JC004393 (2008).
13. S. Haney *et al.*, Hurricane wake restratification rates of one-, two-and three-dimensional processes. *J. Mar. Res.* **70**, 824–850 (2012).
14. C. Pasquero, F. Desbiolles, A. N. Meroni, Air-sea interactions in the cold wakes of tropical cyclones. *Geophys. Res. Lett.* **48**, e2020GL091185 (2021).
15. W. Mei, F. Primeau, J. C. McWilliams, C. Pasquero, Sea surface height evidence for long-term warming effects of tropical cyclones on the ocean. *Proc. Natl. Acad. Sci. U.S.A.* **110**, 15207–15210 (2013).
16. R. L. Sriver, M. Huber, Observational evidence for an ocean heat pump induced by tropical cyclones. *Nature* **447**, 577–580 (2007).
17. K. Emanuel, Contribution of tropical cyclones to meridional heat transport by the oceans. *J. Geophys. Res. Atmos.* **106**, 14771–14781 (2001).
18. L. Cheng, J. Zhu, R. L. Sriver, Global representation of tropical cyclone-induced short-term ocean thermal changes using Argo data. *Ocean Sci.* **11**, 719–741 (2015), 10.5194/os-11-719-2015.
19. R. L. Korty, K. A. Emanuel, J. R. Scott, Tropical cyclone-induced upper-ocean mixing and climate: Application to equable climates. *J. Clim.* **21**, 638–654 (2008).
20. R. L. Sriver, M. Goes, M. E. Mann, K. Keller, Climate response to tropical cyclone-induced ocean mixing in an Earth system model of intermediate complexity. *J. Geophys. Res. Oceans* **115**, e2010JC006106 (2010).
21. A. V. Fedorov, C. M. Brierley, K. Emanuel, Tropical cyclones and permanent El Niño in the early Pliocene epoch. *Nature* **463**, 1066–1070 (2010).
22. R. L. Sriver, M. Huber, Modeled sensitivity of upper thermocline properties to tropical cyclone winds and possible feedbacks on the Hadley circulation. *Geophys. Res. Lett.* **37**, e2010GL042836 (2010).
23. M. R. Bueti, I. Ginis, L. M. Rothstein, S. M. Griffies, Tropical cyclone-induced thermocline warming and its regional and global impacts. *J. Clim.* **27**, 6978–6999 (2014).
24. M. F. Jansen, R. Ferrari, T. A. Mooring, Seasonal versus permanent thermocline warming by tropical cyclones. *Geophys. Res. Lett.* **37**, e2009GL041808 (2010).
25. N. G. Brizuela *et al.*, A vorticity-divergence view of internal wave generation by a fast-moving tropical cyclone: Insights from Super Typhoon Mangkhut. *J. Geophys. Res. Oceans* **128**, e2022JC019400 (2023).
26. J. E. Geisler, Linear theory of the response of a two layer ocean to a moving hurricane. *Geophys. Astrophys. Fluid Dyn.* **1**, 249–272 (1970).
27. M. C. Gregg, E. A. d'Asaro, T. J. Shay, N. Larson, Observations of persistent mixing and near-inertial internal waves. *J. Phys. Oceanogr.* **16**, 856–885 (1986).
28. D. Hebert, J. N. Moum, Decay of a near-inertial wave. *J. Phys. Oceanogr.* **24**, 2334–2351 (1994).

29. Ma. H. Alford, M. C. Gregg, Near-inertial mixing: Modulation of shear, strain and microstructure at low latitude. *J. Geophys. Res. Oceans* **106**, 16947–16968 (2001).
30. R. Hummels *et al.*, Surface cooling caused by rare but intense near-inertial wave induced mixing in the tropical Atlantic. *Nat. Commun.* **11**, 1–13 (2020).
31. Y. Cuypers, X. Le Vaillant, P. Bouruet-Aubertot, J. Vialard, M. J. Mcphaden, Tropical storm-induced near-inertial internal waves during the Cirene experiment: Energy fluxes and impact on vertical mixing. *J. Geophys. Res. Oceans* **118**, 358–380 (2013).
32. M. C. Gregg, Scaling turbulent dissipation in the thermocline. *J. Geophys. Res. Oceans* **94**, 9686–9698 (1989).
33. J. A. MacKinnon, M. C. Gregg, Near-inertial waves on the New England shelf: The role of evolving stratification, turbulent dissipation, and bottom drag. *J. Phys. Oceanogr.* **35**, 2408–2424 (2005).
34. B. Jaimes, L. K. Shay, Near-inertial wave wake of Hurricanes Katrina and Rita over mesoscale oceanic eddies. *J. Phys. Oceanogr.* **40**, 1320–1337 (2010).
35. S. Zhang *et al.*, Tropical storm-induced turbulent mixing and chlorophyll-a enhancement in the continental shelf southeast of Hainan Island. *J. Mar. Syst.* **129**, 405–414 (2014), 10.1016/j.jmarsys.2013.09.002.
36. M. Jansen, R. Ferrari, Impact of the latitudinal distribution of tropical cyclones on ocean heat transport. *Geophys. Res. Lett.* **36**, e2008GL036796 (2009).
37. G. E. Manucharyan, C. M. Brierley, A. V. Fedorov, Climate impacts of intermittent upper ocean mixing induced by tropical cyclones. *J. Geophys. Res. Oceans* **116**, e2011JC007295 (2011).
38. A. H. Sobel *et al.*, Large-scale state and evolution of the atmosphere and ocean during piston 2018. *J. Clim.* **34**, 5017–5035 (2021).
39. G. B. Crawford, W. G. Large, A numerical investigation of resonant inertial response of the ocean to wind forcing. *J. Phys. Oceanogr.* **26**, 873–891 (1996).
40. M. H. Alford, Revisiting near-inertial wind work: Slab models, relative stress, and mixed layer deepening. *J. Phys. Oceanogr.* **50**, 3141–3156 (2020).
41. J. Nilsson, Energy flux from traveling hurricanes to the oceanic internal wave field. *J. Phys. Oceanogr.* **25**, 558–573 (1995).
42. S. W. Chang, R. A. Anthes, Numerical simulations of the ocean's nonlinear, baroclinic response to translating hurricanes. *J. Phys. Oceanogr.* **8**, 468–480 (1978).
43. E. Kunze, Near-inertial wave propagation in geostrophic shear. *J. Phys. Oceanogr.* **15**, 544–565 (1985).
44. L. N. Thomas *et al.*, Direct observations of near-inertial wave ζ-refraction in a dipole vortex. *Geophys. Res. Lett.* **47**, e2020GL090375 (2020).
45. O. Asselin, W. R. Young, Penetration of wind-generated near-inertial waves into a turbulent ocean. *J. Phys. Oceanogr.* **50**, 1699–1716 (2020).
46. M. H. Alford, J. A. MacKinnon, R. Pinkel, J. M. Klymak, Space-time scales of shear in the north pacific. *J. Phys. Oceanogr.* **47**, 2455–2478 (2017).
47. D. F. Leipper, D. Volgenau, Hurricane heat potential of the gulf of Mexico. *J. Phys. Oceanogr.* **2**, 218–224 (1972).
48. L. K. Shay, G. J. Goni, P. G. Black, Effects of a warm oceanic feature on hurricane opal. *Mon. Weather Rev.* **128**, 1366–1383 (2000).
49. L. D. Talley, Shallow, intermediate, and deep overturning components of the global heat budget. *J. Phys. Oceanogr.* **33**, 530–560 (2003).
50. G. Forget, D. Ferreira, Global ocean heat transport dominated by heat export from the tropical pacific. *Nat. Geosci.* **12**, 351–354 (2019).
51. D. Roemmich, J. Gilson, Eddy transport of heat and thermocline waters in the north pacific: A key to interannual/decadal climate variability? *J. Phys. Oceanogr.* **31**, 675–687 (2001).
52. R. L. Sriver, M. Huber, J. Nusbaumer, Investigating tropical cyclone-climate feedbacks using the TRMM microwave imager and the quick scatterometer. *Geochem. Geophys. Geosyst.* **9**, e2007GC001842 (2008).
53. M. Claret, M.-P. Lelong, K. B. Winters, Y. Ourmières, "Wave-eddy interactions in the gulf of lion: Bridging ocean general circulation models and process ocean simulations" (Tech. rep., Copernicus Meetings, 2022).
54. R. E. Hart, An inverse relationship between aggregate northern hemisphere tropical cyclone activity and subsequent winter climate. *Geophys. Res. Lett.* **38**, e2010GL045612 (2011).
55. K. J. E. Walsh, M. Fiorino, C. W. Landsea, K. L. McInnes, Objectively determined resolution-dependent threshold criteria for the detection of tropical cyclones in climate models and reanalyses. *J. Clim.* **20**, 2307–2314 (2007).
56. E. M. Vincent *et al.*, Processes setting the characteristics of sea surface cooling induced by tropical cyclones. *J. Geophys. Res. Oceans* **117**, e2011JC007396 (2012).
57. K. D. Leaman, T. B. Sanford, Vertical energy propagation of inertial waves: A vector spectral analysis of velocity profiles. *J. Geophys. Res.* **80**, 1975–1978 (1975).
58. D. Roemmich, J. Gilson, The 2004–2008 mean and annual cycle of temperature, salinity, and steric height in the global ocean from the Argo program. *Prog. Oceanogr.* **82**, 81–100 (2009).
59. M. H. Alford, A. Y. Shcherbina, M. C. Gregg, Observations of near-inertial internal gravity waves radiating from a frontal jet. *J. Phys. Oceanogr.* **43**, 1225–1239 (2013).
60. J. N. Moum, M. C. Gregg, R. C. Lien, M. E. Carr, Comparison of turbulence kinetic energy dissipation rate estimates from two ocean microstructure profilers. *J. Atmos. Ocean. Technol.* **12**, 346–366 (1995).
61. T. R. Osborn, Estimates of the local rate of vertical diffusion from dissipation measurements. *J. Phys. Oceanogr.* **10**, 83–89 (1980).
62. J. N. Moum, Efficiency of mixing in the main thermocline. *J. Geophys. Res. Oceans* **101**, 12057–12069 (1996).
63. W. D. Smyth, J. N. Moum, D. R. Caldwell, The efficiency of mixing in turbulent patches: Inferences from direct simulations and microstructure observations. *J. Phys. Oceanogr.* **31**, 1969–1992 (2001).
64. W. C. Skamarock *et al.*, A description of the Advanced Research WRF version 3. NCAR Technical note-475+ STR (2008).
65. E. P. Chassignet *et al.*, The HYCOM (hybrid coordinate ocean model) data assimilative system. *J. Mar. Syst.* **65**, 60–83 (2007).
66. D. B. Chelton, R. A. DeSzoeke, M. G. Schlax, K. El Naggar, N. Siwertz, Geographical variability of the first baroclinic Rossby radius of deformation. *J. Phys. Oceanogr.* **28**, 433–460 (1998).
67. N. G. Brizuela *et al.*, Observational data for "Prolonged thermocline warming by near-inertial internal waves in the wake of tropical cyclones." Zenodo. https://zenodo.org/record/7601193. Deposited 2 February 2023.